

MIT Open Access Articles

*Quantum reference beacon-guided
superresolution optical focusing in complex media*

The MIT Faculty has made this article openly available. **Please share**
how this access benefits you. Your story matters.

Citation: Kim, Donggyu and Dirk R. Englund. "Quantum reference beacon-guided superresolution optical focusing in complex media." *Science* 363, 6426 (February 2019): 528-531
© 2019 American Association for the Advancement of Science

As Published: <http://dx.doi.org/10.1126/science.aar8609>

Publisher: American Association for the Advancement of Science (AAAS)

Persistent URL: <https://hdl.handle.net/1721.1/121337>

Version: Original manuscript: author's manuscript prior to formal peer review

Terms of use: Creative Commons Attribution-Noncommercial-Share Alike



Quantum Reference Beacon-Guided Super-Resolution Optical Focusing in Complex Media

Donggyu Kim^{1,2,*} and Dirk R. Englund^{2,3}

¹*Department of Mechanical Engineering, Massachusetts Institute of Technology,
77 Massachusetts Avenue, Cambridge, MA, 02139, USA*

²*Research Laboratory of Electronics (RLE), Massachusetts Institute of Technology,
50 Vassar Street, Cambridge, MA, 02139, USA*

³*Department of Electrical Engineering and Computer Science,
Massachusetts Institute of Technology, 50 Vassar Street, Cambridge, MA, 02139, USA*

Optical random scattering is generally considered to be a nuisance of microscopy that limits imaging depth and spatial resolution. Wavefront shaping techniques have recently enabled optical imaging at unprecedented depth, but a remaining problem is also to attain super-resolution within complex media. To address this challenge, we introduce a new technique to focus inside of complex media by the use of a quantum reference beacon (QRB), consisting of solid-state quantum emitters with spin-dependent fluorescence. This QRB provides subwavelength guidestar feedback for wavefront shaping to achieve an optical focus below the microscope's diffraction limit. We implement the QRB-guided imaging approach using nitrogen-vacancy centers in diamond nanocrystals, which enable optical focusing with a subdiffraction resolution below 186 nm ($\approx \lambda/3.5\text{NA}$), where the microscope's NA=0.8. This QRB-assisted wavefront shaping paves the way for a range of new applications, including deep-tissue quantum enhanced sensing and individual optical excitation of magnetically-coupled spin ensembles for applications in quantum information processing.

Optical random scattering in complex media, such as biological tissues, distorts an incident optical focus, reducing the resolution and imaging depth of optical microscopy. However, it was recently shown that random scattering does not lead to the permanent loss of focusing capability; instead it randomizes the incident focus in a deterministic way. By reversing this scattering, it becomes possible to focus¹⁻³ and even to image⁴⁻⁶ through complex media. Moreover, random scattering can actually benefit^{1-3,5,6} microscopy by permitting a spatial resolution below the diffraction-limit of $\lambda/2\text{NA}$, where NA is the numerical aperture of the microscope objective. This super-resolution is possible because random scattering couples optical modes with high in-plane momentum from the sample to the microscope objective, much like a disordered grating. By extending this principle to evanescent modes of the sample, far-field superlenses for near-field focusing³ and imaging⁶ have been achieved.

Reversing random scattering requires feedback from the target focal points. In particular, focusing light inside of complex media requires a type of "guidestar (GS)" that provides feedback of the interior optical field⁷. This feedback guides incident wavefront adjustments to focus the scattered light into the GS point. In the last decade, various forms of GSs have been implemented, including fluorescence⁸, ultrasound⁹⁻¹⁴, nonlinear reference beacons¹⁵, and kinetic objects^{16,17}. However, the spatial resolution using these types of GSs has been far from the super-resolution limit⁷. To push this resolution to or below the diffraction limit requires two key advances: (i) the physical size of the GS needs to be of subwavelength scale, and (ii) it must be possible to resolve subdiffraction features of randomly scattered light^{3,6}. A

subwavelength aperture used in scanning near-field optical microscopy (SNOM) satisfies these conditions, but this technique does not permit imaging within a complex medium. To address these challenges, we introduce quantum reference beacons (QRBs).

The QRB we propose consists of solid-state quantum emitters with spin-dependent fluorescence. An example is the nitrogen vacancy (NV) center in diamond, which has emerged as a leading quantum system for quantum sensing¹⁸⁻²⁰ and quantum information processing²¹⁻²⁷. By resonantly driving electron spin transitions of each QRB, the spin-dependent fluorescence produces the subwavelength GS feedback that enables super-resolution focusing within complex media. We demonstrate our proposal with ensembles of NV centers in subwavelength diamond nanocrystals, and show super-resolution focusing inside of a disordered scattering medium with a resolution below 186 nm ($\approx \lambda/3.5\text{NA}$ with $\lambda = 532$ nm).

Figure 1 illustrates the approach to QRB-guided wavefront shaping in microscopy. A wavefront shaper adjusts basis modes (shown as individual pixels in Fig. 1A) of the incident wavefront to interfere scattered light constructively at target GS points. This specific wavefront adjustment is determined from the QRB-GS feedback. This feedback signal is created by applying a magnetic field gradient across the sample so that one of several QRBs inside a diffraction-limited volume can be selectively driven into its dark magnetic sublevels, as indicated in Fig. 1C and detailed below.

Specifically, the QRB-GS feedback signal is needed to measure the transmission matrix⁷ that characterizes the light propagation through a complex medium (See Supplementary text S1 and S2 for details). We label the electron spin state of the embedded QRBs at $\{\mathbf{x}_i\} = \mathbf{x}_1, \dots, \mathbf{x}_N$ with a spin density operator $\rho = \rho_1 \otimes \rho_2 \otimes \dots \otimes \rho_N$. An external magnetic field gradient separates their resonance frequencies $\{\nu_i\}$ by the Zee-

* donggyu@mit.edu

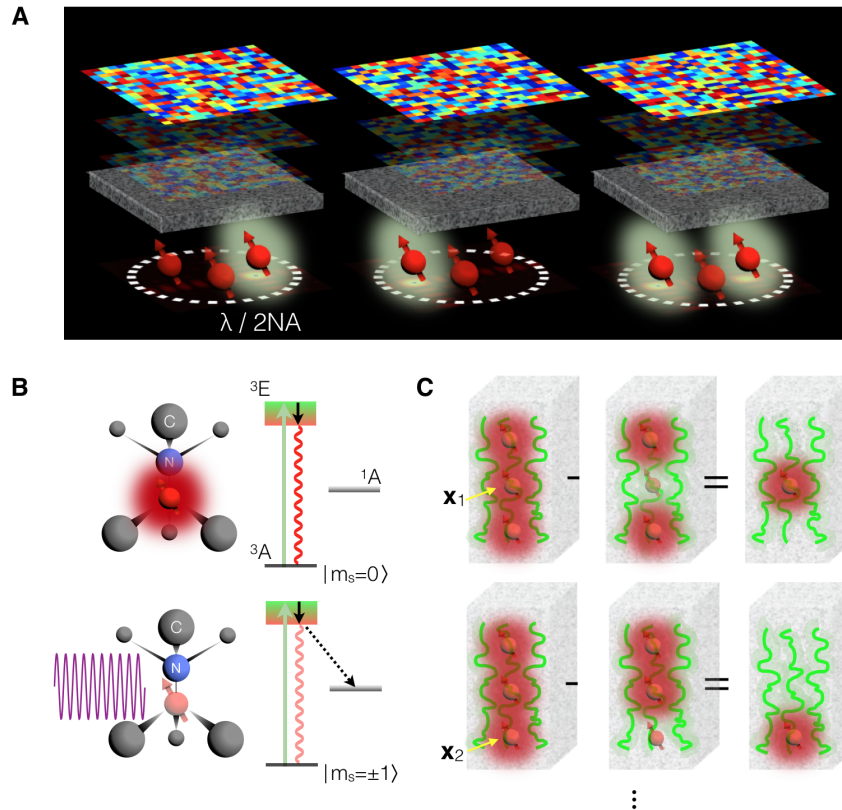


FIG. 1. **Wavefront shaping guided by quantum reference beacons (QRBs)** (A) Optical random scattering in complex media distorts the incident optical field. However, this distortion can be reversed by shaping the incident wavefront. Embedded QRBs provide feedback about subwavelength features of the scattered optical fields, guiding the wavefront shaping process. This approach enables, for example, super-resolution focusing deep inside of complex media or individual spin-qubit measurement in a diffraction-limited area (the dashed circle). (B) Nitrogen-vacancy (NV) centers in diamond with spin-dependent fluorescence: Electrons with the spin magnetic sublevels $|m_s = \pm 1\rangle$ preferentially decay (dashed black arrow) to the dark metastable state (1A), once they are optically pumped to the excited states 3E (green arrow), resulting in reduced fluorescence than that from the sublevel $|m_s = 0\rangle$. This spin-dependent fluorescence enables optically detectable magnetic resonance (ODMR). (C) The QRB-GS feedback is produced with the spin-dependent fluorescence: To measure the optical field on the QRB positioned at \mathbf{x}_1 , its fluorescence is selectively reduced by electron spin resonance (ESR). The change of collected fluorescence determines the optical field at \mathbf{x}_1 . This process can be repeated for another position at \mathbf{x}_2 as shown in the bottom plot.

man effect. In principle, $\{\mathbf{x}_i\}$ could then be reconstructed from $\{\nu_i\}$ and knowledge of the external magnetic field gradient. Resonant driving of each $\{\rho_i\}$ spin transition is represented through a quantum operator $\{E_i\}$. When the j th incident basis mode is coupled into the medium, the QRB-GS feedback $S_{i,j}$ for \mathbf{x}_i is described by

$$S_{i,j} = N_j[\boldsymbol{\rho}] - N_j[E_i(\boldsymbol{\rho})] = |t_{i,j}|^2 \Delta\sigma_i \Delta\gamma. \quad (1)$$

Here, $N_j[\boldsymbol{\rho}]$ and $N_j[E_i(\boldsymbol{\rho})]$ denote the fluorescence photon numbers collected for unit integration, $t_{i,j}$ is the transmission matrix element (i.e. the scattered optical field at \mathbf{x}_i for the j th incident basis mode), $\Delta\sigma_i = \frac{1}{2}\text{tr}[\sigma_z\{\rho_i - E_i(\rho_i)\}]$ where σ_z is the Pauli- z operator, and $\Delta\gamma$ represents the variance of the collected spin-dependent fluorescence between the optically bright and dark spin states (Fig. 1B). Figure 2 summarizes the iterative wavefront adjustments due to the QRB-GS feedback.

The spatial resolution of our method is determined by the ESR lineshape (See Supplementary text S2 for

details), since the lineshape sets the point spread function (PSF) of the QRB-GS feedback that confines $\{E_i\}$ only to the target QRBs (Fig. 2A). Specifically, a magnetic field gradient dB/dx translates the (mean) resonance linewidth $\delta\nu$ to the spatial resolution Δd_{QRB} of the effective PSF:

$$\Delta d_{\text{QRB}} = \frac{\delta\nu}{\gamma_e(dB/dx)} \quad (2)$$

where γ_e is the gyromagnetic ratio of the electronic spin ($\simeq 2.8$ MHz/Gauss). Combined with the crystal-orientation-dependent Zeeman splitting and dynamical decoupling to narrow the linewidth, this resolution can go down to a few tens of nanometers^{28,29}.

Figure 3 illustrates the experimental configuration for demonstrating QRB-assisted wavefront shaping. Our QRBs consist of ensembles of NV centers (Fig. 1B) in nanodiamonds with a mean diameter of 50 nm. The QRBs are embedded in a complex medium consisting of

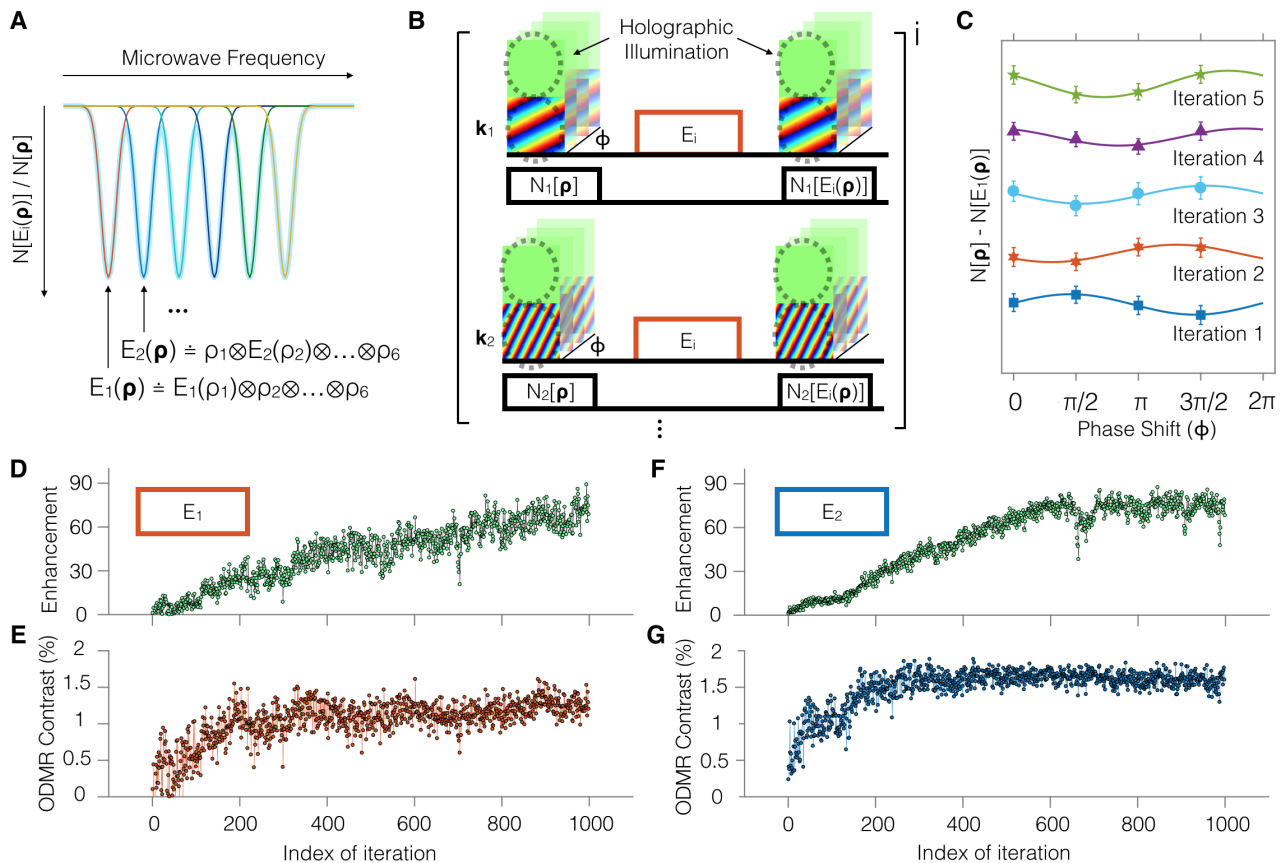


FIG. 2. **Iterative wavefront optimization with QRB-GS feedback.** (A) $\{\rho_i\}$ label the electron spin states of QRBs, and an external magnetic field gradient splits their individual resonance frequencies. Quantum operators $\{E_i\}$ drive the electron spin transition of target QRBs. (B) Measurement sequences for the iterative wavefront optimization: the Fourier basis modes of the incident wavefront ($\mathbf{k}_1, \mathbf{k}_2, \dots$) are encoded into holographic illuminations, in which the basis modes interfere with the reference plane wave for complex field readout (See Supplementary text S4 and S5 for details). The overall fluorescence difference with $\{E_i\}$ (i.e. $N_j[\rho] - N_j[E_i(\rho)]$) produces the QRB-GS feedback $S_{i,j}$. ϕ describes the phase of each basis mode relative to the reference plane wave. (C) Modulation of the QRB-GS feedback in the iterative wavefront optimization: In each step, the phase ϕ of the basis modes is adjusted to compensate for the phase offset of the modulation. (D) and (F) The iterative wavefront optimization with the QRB-GS feedback: Two QRBs have the electron spin resonance frequencies at $\nu_1 = 2.825$ GHz and $\nu_2 = 2.762$ GHz. The resonant microwaves continuously drive the resonances to produce the QRB-GS feedback, so that the incident optical fields can be iteratively updated to optimize the QRB-GS feedback signal strength. (E) and (G) The ODMR contrast at ν_1 and ν_2 for the iterative optimization processes.

randomly distributed TiO_2 nanoparticles with a mean diameter of 21 nm. The incident green laser light ($\lambda = 532$ nm) is randomly scattered as it propagates through the medium. This scattering produces subwavelength spatial features on the incident laser light^{3,30}, which excite the embedded QRBs. In particular, we demonstrate super-resolution focusing on two QRBs at \mathbf{x}_1 (QRB₁) and \mathbf{x}_2 (QRB₂) in Fig. 3C, where their separation $|\mathbf{x}_1 - \mathbf{x}_2| = 186$ nm is far below the diffraction limit of our excitation objective lens, 406 nm (Fig. S3). The QRB₁ (QRB₂) has the ESR frequency of $\nu_1 = 2.825$ GHz ($\nu_2 = 2.762$ GHz), which corresponds to the electronic spin transition between $|m_s = 0\rangle$ and one of the Zeeman-split $|m_s = \pm 1\rangle$ of the ground spin triplet (³A, Fig. 1B). Since ν_1 and ν_2 are well-separated ($\Delta\nu \simeq 63$ MHz) compared to their resonance linewidths ($\delta\nu_1 = 5$ MHz and $\delta\nu_2 = 5.6$ MHz), it is possible to individually drive the

spin transition of each QRB.

In this study, we shape the incident wavefront with 793 transverse Fourier basis modes $\{\mathbf{k}_n\}$, which cover the entire back aperture of the excitation objective. Resonant microwaves drive the spin transitions at ν_1 and ν_2 that produce the QRB-GS feedback, and the phase of $\{\mathbf{k}_n\}$ is iteratively adjusted to optimize the feedback signal (Fig. 2D and 2F). Figure 4A and 4B plot the results of the wavefront optimizations W_{ν_1} and W_{ν_2} , respectively. For comparison, Fig. 4C shows the wavefront W_{cl} , obtained without the use of ESR (i.e. by optimizing only fluorescence feedback from QRBs). This fluorescence GS method^{7,8} focuses the interior optical field without achieving super-resolution.

Projecting the wavefronts W_{ν_1} (W_{ν_2}) forms a super-resolution optical focus at \mathbf{x}_1 (\mathbf{x}_2) in the complex medium. We can verify this super-resolution focusing

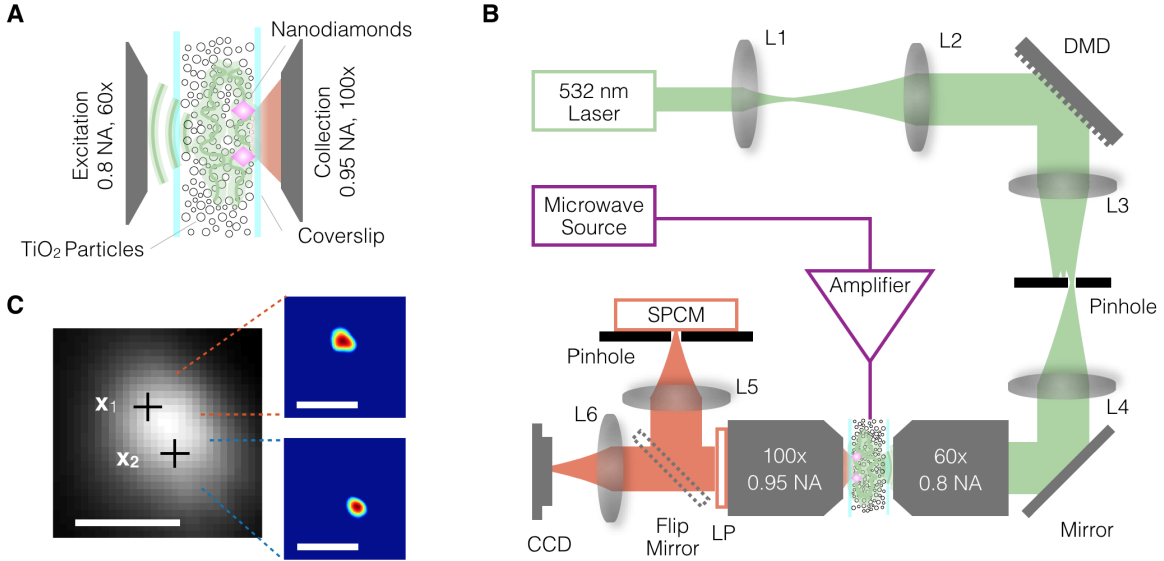


FIG. 3. Experimental Configuration. (A) NV centers in subwavelength nanodiamonds (Diamond Nanotechnologies) are embedded in a complex medium consisting of randomly distributed TiO_2 nanoparticles (Sigma Aldrich 718467). A green laser beam is delivered to the complex medium by a microscope objective (0.8 NA, 60x). An objective (0.95 NA, 100x) at the other side directly collects spin-dependent broadband red fluorescence from NV centers. The thickness of the complex medium is $\sim 7 \pm 2 \mu\text{m}$. (B) Setup schematic: A DMD shapes the wavefront of the incident green laser and projects it onto the back aperture of excitation objective. The phase of each incident basis mode $\{\mathbf{k}_n\}$ is controlled by groups of 24 by 24 DMD micro-mirrors. SPCM (CCD) counts (images) the red fluorescence collected by the collection objective. LP rejects the transmitted green laser, and a pinhole in front of SPCM blocks stray red fluorescence. A copper wire (diameter of $25 \mu\text{m}$) delivers the microwave signal to QRBs to modulate their spin ground state population. A permanent magnet (not shown) separates the magnetic resonance frequencies of the QRBs by orientation-dependent Zeeman splitting. (DMD: a digital micro-mirror device, SPCM: a single photon counting module, CCD: a charge-coupled device, LP: a long-pass optical filter with a cutoff wavelength of 650 nm , and L1 - L6: lens) (C) QRb fluorescence images for super-resolution focusing demonstration. \mathbf{x}_1 and \mathbf{x}_2 denote the QRb positions. Inset images are obtained using super-resolution focusing of our QRb-assisted wavefront shaping technique. (All scale bars = $0.61\lambda/\text{NA}$ with $\text{NA} = 0.8$ and $\lambda = 532 \text{ nm}$)

by investigating optically-detectable-magnetic-resonance (ODMR) spectra. This is because (i) ODMR spectra exhibit resonances only of optically pumped QRBs, and (ii) QRB_1 and QRB_2 have distinguishable spectra. Figure 4D plots the ODMR spectra for this investigation. First, we project the wavefront W_{cl} with the DMD (Fig. 3B), which produces the ODMR spectrum shown in the black line. This spectrum shows the resonances at ν_1 and ν_2 of both QRBs, as expected. By contrast, the only resonance of QRB_1 appears (the Red line) when we project W_{ν_1} , which is obtained using the QRb-GS feedback with the spin transition at ν_1 . Alternatively, projecting W_{ν_2} reveals the resonance of QRB_2 (the Blue lines). This demonstration validates the ability of QRb-guided wavefront shaping to enable optical addressing of individual spots far below the diffraction limit. Note that the resonance linewidths are slightly broadened when the QRBs are excited by the targeted subwavelength foci, owing to the optically induced relaxation of ODMR³¹.

The ODMR spectra with subwavelength spin addressing enable us to estimate the spatial resolutions of the optical foci (Fig. 4E). We determine the peak-to-background intensity ratio of the focus (i.e. $I(\mathbf{x}_1)/I(\mathbf{x}_2)$ or vice versa) from the ODMR spectra (See Supplementary text S6 for details). Assuming the subwavelength fo-

cus features a Gaussian intensity envelop, the intensity ratio indicates that the super-resolution focus at \mathbf{x}_1 (\mathbf{x}_2) has a spatial resolution of 204 nm (184 nm). This achieved resolution is 2 (2.21) times smaller than our diffraction-limited resolution and 1.31 (1.45) times smaller than the far-field-limited one ($\text{NA} = 1$).

In conclusion, we introduced a quantum reference beacon (QRb) that enables super-resolution optical focusing within complex media. This QRb-GS approach uniquely provides, for the first time, sub-wavelength guidestar feedback inside a scattering medium by the use of spin coherence. Implementing our proposal with NV centers demonstrates clear super-resolution focusing capabilities inside of a complex medium. This QRb-assisted wavefront shaping opens up a range of applications. First, it can extend to quantum sensing based on NV centers to greater imaging depth and optical super-resolution. Second, it can be used to characterize the light propagation through a fiber for single-fiber endomicroscopy³². Finally, our method could open up the way for subwavelength optical spin measurement^{33,34} of magnetic dipole-coupled quantum emitters²⁸, which is essential for advanced quantum sensing³⁵, quantum error correction²⁵, and room-temperature quantum computing³⁶.

The authors would like to thank Noel H. Wan for

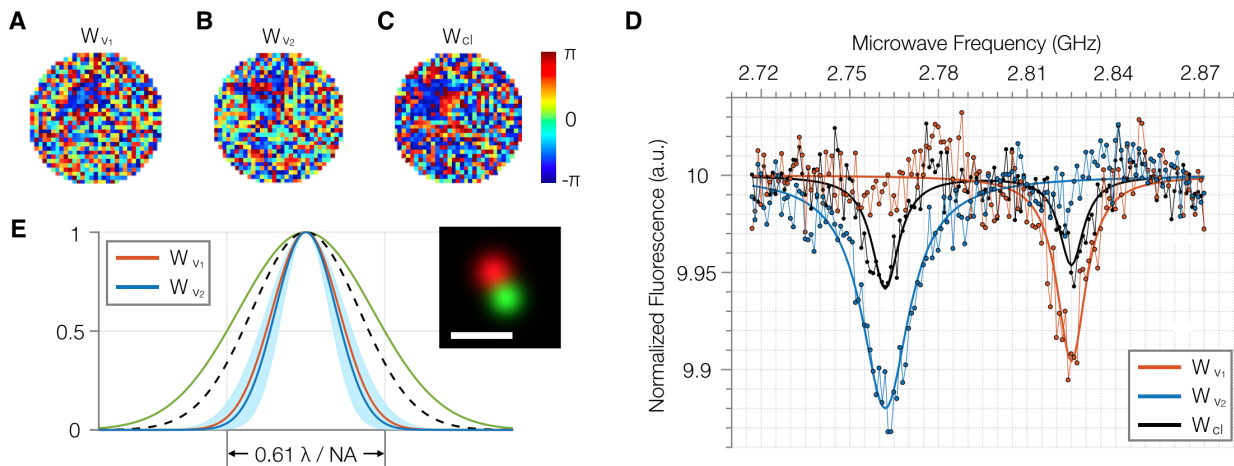


FIG. 4. **Subwavelength optical focusing in a complex medium.** (A) and (B) The phase-only wavefronts W_{ν_1} and W_{ν_2} , determined by optimizing the QRB-GS feedback at ν_1 and ν_2 , respectively. (C) The phase-only wavefront W_{cl} , obtained using the fluorescence GS method. (D) ODMR spectra with W_{ν_1} (Red), W_{ν_2} (Blue), and W_{cl} (Black) projection. (E) Spatial resolution of the subwavelength foci in the complex medium: The Red and Blue lines plot the estimated intensity shape of the subwavelength foci with W_{ν_1} and W_{ν_2} projection, respectively. The shaded area gives the estimation uncertainty. The Green line plots the point spread function (PSF) of the excitation objective (FWHM = $0.61\lambda/NA$ with $\lambda = 532$ nm and $NA = 0.8$), and the Black dashed line refers to the far-field limited PSF ($NA = 1$). Inset: reconstructed image of the subwavelength foci with W_{ν_1} (Red) and W_{ν_2} (Green). (Scale bar = $0.61\lambda/NA$ with $NA = 0.8$ and $\lambda = 532$ nm)

his perspective on the manuscript. Donggyu Kim acknowledges financial support from Kwanjeong Educational Foundation. This research is supported in part by the Army Research office MURI biological transduction program and NSF Center for Integrated Quantum Materials.

SUPPLEMENTARY TEXT

S1. Electronic Spin Resonance of Quantum Reference Beacons

The quantum reference beacon (QRB) consists of a solid-state quantum emitter with spin-dependent fluorescence. One example is a nitrogen-vacancy (NV) center in diamond, which has the electron spin magnetic sublevels $|m_s = \pm 1\rangle$ that are optically darker than $|m_s = 0\rangle$ ³⁷. This spin-dependent fluorescence enables optical detection of magnetic resonance. The QRB-guidestar feedback is based on the optically detectable magnetic resonance (ODMR), in which we readout the optical fields at the resonance points inside of complex media. By driving the resonances of the QRBs, we individually modulate their spin populations below the optical diffraction-limited resolution, which produces the guidestar feedback for wavefront shaping. In our NV-based experiment, we drive the resonance between the bright $|m_s = 0\rangle$ and one of the dark $|m_s = \pm 1\rangle$ of NV centers. In the following, we represent the bright and dark spin state involved in the magnetic resonance as $|0\rangle$ and $|1\rangle$, respectively, and denote a spin state of a QRB with a spin density operator ρ .

For our QRB-assisted wavefront shaping, the evolution of ρ is described by the master equation

$$\frac{d\rho}{dt} = \frac{1}{i\hbar}[H, \rho] + \left\{ \frac{d\rho}{dt} \right\}_{\text{relax}}, \quad (\text{S1})$$

where H is a simple two-level spin Hamiltonian that describes the relevant interaction of QRB with a microwave:

$$H = \hbar\omega |1\rangle\langle 1| + \hbar\Omega \cos(\omega_{\text{mw}})(|0\rangle\langle 1| + |1\rangle\langle 0|).$$

Here, the energy splitting $\hbar\omega$ includes the zero-field splitting $D_{\text{gs}} \simeq 2.87$ GHz and the electronic Zeeman splitting $\gamma_e B_{0z}$, where $\gamma_e = 2.8$ MHz / Gauss and B_{0z} is a magnetic field along the symmetry axis of NV centers³⁷. ω_{mw} is a microwave frequency that drives the magnetic resonance with the Rabi frequency Ω .

The last term of the master equation Eq. (S1) represents the spin relaxation due to the interaction with the QRB's environment. This relaxation process includes the intrinsic spin relaxation from magnetic dipolar interactions with a spin bath. In addition, optical excitation induces spin relaxation through (i) spin polarization via intersystem crossing (ISC) followed by non-radiative decay, and (ii) the decoherence with scattered photons³¹. Typical values of the intrinsic and optically induced relaxation rates for NV centers can be found in A. Dréau *et al.*³¹

Modulating the spin state ρ with a resonant microwave produces the guidestar feedback (the QRB-GS feedback). We denote the modulation through a quantum operator E that maps an initial spin state ρ to the modulated state $E(\rho)$. In our experiment, we modulate ρ by continuous ESR (electronic spin resonance) spectroscopy, in which ρ

and $E(\rho)$ are the steady-state solutions of Eq. (S1) under optical excitation. With the modulation, the change of the spin population $\Delta\sigma$ is

$$\Delta\sigma = \frac{1}{2}\text{tr}[\sigma_z\{\rho - E(\rho)\}], \quad (\text{S2})$$

where σ_z is the Pauli- z operator, and $\text{tr}[\cdot]$ is the trace operator. For example, $\Delta\sigma = 1/2$ for continuously-driven ESR of an initially polarized spin (i.e. $\rho = |0\rangle\langle 0|$), and $\Delta\sigma = 1$ for an ideal spin flip with a microwave π -pulse. For the case that the microwave has a detuning δ from the spin resonance frequency, $\Delta\sigma$ is reduced by an ESR lineshape $g(\delta)$ with $g(0) = 1$:

$$\frac{1}{2}\text{tr}[\sigma_z\{\rho_\delta - E(\rho_\delta)\}] = g(\delta)\Delta\sigma. \quad (\text{S3})$$

Here, ρ_δ refers to the spin state that is driven by the microwave with a detuning of δ . Although details of the lineshape function depend on the dominant broadening mechanisms, we assume here that $g(\delta)$ is a Gaussian-shape function with a full-width-at-half-maximum (FWHM) linewidth of $\delta\nu$.

S2. The QRB-Guidestar Feedback

In this section, we formulate the QRB-GS feedback in detail. As introduced in the main manuscript, $\boldsymbol{\rho} = \rho_1 \otimes \cdots \otimes \rho_M$ labels the initial spin state of QRBs at positions of $\mathbf{x}_1, \cdots, \mathbf{x}_M$ inside of the complex medium. An external magnetic field gradient separates individual resonance frequencies $\{\nu_m\}$ of $\{\rho_m\}$ ($m = 1, 2, \cdots, M$). $\{E_m\}$ resonantly modulate the spin density operators $\{\rho_m\}$ with lineshape functions $\{g_m\}$ and linewidths $\{\delta\nu_m\}$. In principle, $\{\mathbf{x}_m\}$ could then be reconstructed from $\{\nu_m\}$ and knowledge of the external magnetic field.

Optical fields inside of the complex medium are described by a transmission matrix \mathbf{T} . For example, the matrix element $t_{m,n}$ describes the optical field at $\{\mathbf{x}_m\}$ when the n th incident basis mode couples into the medium³⁸, i.e., $|t_{m,n}|^2$ is the optical intensity that excites the QRB at \mathbf{x}_m . The internal optical fields excite the embedded QRBs, which in turn emit spin-dependent broadband fluorescence. By driving the spin resonance of target QRBs, the spin-dependent fluorescence provides information of the transmission matrix elements.

Specifically, obtaining the QRB-GS feedback $S_{i,n}$ at \mathbf{x}_i for the n th incident basis mode proceeds as follow. We first collect the fluorescence photons of the initial spin state $\boldsymbol{\rho}$ with the basis mode. The photon numbers N_n collected for unit integration time is:

$$N_n[\boldsymbol{\rho}] = \sum_m^M |t_{m,n}|^2 \{\gamma_0\sigma_{00}^m + \gamma_1\sigma_{11}^m\}. \quad (\text{S4})$$

Here, γ_0 (γ_1) represents the collected spin-dependent photon numbers of $|0\rangle$ ($|1\rangle$) for unit excitation intensity. σ_{00}^m and σ_{11}^m account for the spin population (i.e.

$\sigma_{00}^m = \langle 0|\rho_m|0\rangle$, $\sigma_{11}^m = \langle 1|\rho_m|1\rangle$) of the QRBs. We assume that the photon collection are identical for all embedded QRBs.

Next, we apply a microwave that is resonant to the target i th-QRB and repeat the fluorescence photon collection. As introduced in Eq. (S2) and (S3), the microwave operation, which is represented through a quantum operator E_i , modulates the spin population by $\Delta\sigma_i$ for the target QRB and by $g_m(\delta_m^i)\Delta\sigma_m$ for the other ‘background’ m th-QRB, where $\delta_m^i = \nu_m - \nu_i$ (i.e. $\delta_i^i = 0$). Then the collected photon number N_n is

$$\begin{aligned} N_n[E_i(\boldsymbol{\rho})] &= |t_{i,n}|^2 \{\gamma_0(\sigma_{00}^i - \Delta\sigma_i) + \gamma_1(\sigma_{11}^i + \Delta\sigma_i)\} \\ &+ \sum_{m \neq i}^M |t_{m,n}|^2 \{\gamma_0(\sigma_{00}^m - g_m(\delta_m^i)\Delta\sigma_m) \\ &+ \gamma_1(\sigma_{11}^m + g_m(\delta_m^i)\Delta\sigma_m)\}. \end{aligned} \quad (\text{S5})$$

By subtracting Eq. (S5) from (S4),

$$\begin{aligned} N_n[\boldsymbol{\rho}] - N_n[E_i(\boldsymbol{\rho})] &= |t_{i,n}|^2 \Delta\sigma_i(\gamma_0 - \gamma_1) \\ &+ \sum_{m \neq i}^M |t_{m,n}|^2 g_m(\delta_m^i)\Delta\sigma_m(\gamma_0 - \gamma_1). \end{aligned} \quad (\text{S6})$$

If $\delta_m^i \geq \delta\nu_m$ for all $m \neq i$, the contribution from the background QRBs is ignorable, reducing Eq. (S6) to the desirable QRB-GS feedback at \mathbf{x}_i :

$$S_{i,n} = N_n[\boldsymbol{\rho}] - N_n[E_i(\boldsymbol{\rho})] = |t_{i,n}|^2 \Delta\sigma_i(\gamma_0 - \gamma_1).$$

The condition $\delta_m^i \geq \delta\nu_m$ determines our spatial resolution of the QRB-GS feedback, with an analogous to Rayleigh resolution limit in conventional optical microscopy. For a given external magnetic field gradient dB/dx , the ESR lineshape $g(\delta_m^i)$ is translated to an effective point spread function (PSF) of the QRB-GS feedback. Thus, our spatial resolution Δd_{QRB} is given by the FWHM resolution of the effective PSF:

$$\Delta d_{\text{QRB}} = \frac{\delta\nu}{\gamma_e(dB/dx)}.$$

Here, $\delta\nu$ is the mean ESR linewidth of QRBs (i.e. $\frac{1}{M} \sum_{m=1}^M \delta\nu_m$). This spatial resolution can be improved by introducing assumptions such as $\Delta\sigma_1 = \Delta\sigma_2 = \cdots = \Delta\sigma_M$. This resolution improvement depends on the accuracy of the assumptions and the signal-to-noise ratio of the measurements as in conventional optical microscopy³⁹.

S3. Noise Estimation

The noise in the QRB-GS feedback can be modeled with the photon shot noise of spin-dependent fluorescence. For the QRB-GS feedback

$$S_{i,n} = N_n[\boldsymbol{\rho}] - N_n[E(\boldsymbol{\rho})] = |t_{i,n}|^2 \Delta\sigma_i(\gamma_0 - \gamma_1), \quad (\text{S7})$$

we consider the photon shot noise in $N_n[\boldsymbol{\rho}]$ and $N_n[E(\boldsymbol{\rho})]$:

- $|t_{i,n}| \sqrt{\gamma_0 \sigma_{00}^i + \gamma_1 \sigma_{11}^i}$
- $|t_{i,n}| \sqrt{\gamma_0 (\sigma_{00}^i - \Delta \sigma_i) + \gamma_1 (\sigma_{11}^i + \Delta \sigma_i)}$
- $\sum_{m \neq i}^M |t_{m,n}| \sqrt{\gamma_0 \sigma_{00}^m + \gamma_1 \sigma_{11}^m}$
- $\frac{\sum_{m \neq i}^M |t_{m,n}|}{\sqrt{\gamma_0 \{\sigma_{00}^m - g_m(\delta_m^i) \Delta \sigma_m\} + \gamma_1 \{\sigma_{11}^m + g_m(\delta_m^i) \Delta \sigma_m\}}}$

Assuming that the complex medium is in a lossless waveguide whose cross-section area is A , the noise $N_{i,n}$ to signal Eq. (S7) ratio is

$$\begin{aligned} \frac{N_{i,n}}{S_{i,n}} &= \frac{\sum_m |t_{m,n}| \sqrt{1 - \sigma_{11}^m C}}{|t_{i,n}|^2 \Delta \sigma_i \sqrt{\gamma_0 C}} \\ &\quad \times \left[1 + \sqrt{1 - \frac{\Delta \sigma_m g_m(\delta_m^i) C}{1 - \sigma_{11}^m C}} \right] \\ &\simeq \frac{\sum_m |t_{m,n}| \sqrt{1 - \sigma_{11}^m C}}{|t_{i,n}|^2 \Delta \sigma_i \sqrt{\gamma_0 C}} \\ &\quad \times \left[2 - \frac{\Delta \sigma_m g_m(\delta_m^i) C}{2(1 - \sigma_{11}^m C)} \right] \\ &\lesssim \frac{2 \sum_m |t_{m,n}|}{|t_{i,n}|^2 \Delta \sigma_i \sqrt{\gamma_0 C}} \\ &\simeq \frac{2M \sqrt{(a/A)T}}{(a/A)T \Delta \sigma_i \sqrt{\gamma_0 C}} \\ &= \frac{2M}{\sqrt{\gamma_0} \tilde{a} T \Delta \sigma_i C}. \end{aligned}$$

Here, $\sum_{m=1}^M |t_{m,n}|^2 = (a/A)T \doteq \tilde{a}T$ where a is the cross-sectional area of QRBs, $C = 1 - \gamma_1/\gamma_0$, and T is the total transmission of the complex medium. As expected, the noise-to-signal ratio approaches to zero for a longer integration.

S4. Four-Phase Method with the QRB-GS Feedback

To access the phase of the transmission matrix element $t_{m,n}$, the incident Fourier basis modes $\{\mathbf{k}_n\}$ are encoded into the holographic illuminations by interfering themselves with the reference mode u_{ref} . Specifically, the holographic illumination of a incident basis mode \mathbf{k}_n is represented by

$$E_n^{\text{in}}(\phi) = 1 + e^{i(\mathbf{k}_n \cdot \mathbf{r} + \phi)}, \quad (\text{S8})$$

where we choose $u_{\text{ref}} = 1$, and ϕ is the phase of the basis mode relative to the reference mode. When $E_n^{\text{in}}(\phi)$ couples to the complex medium, the scattered optical field on the i th QRB is⁴⁰

$$\begin{aligned} E_{i,n}^{\text{out}}(\phi) &= \mathbf{T} E_n^{\text{in}} = t_{i,R} + t_{i,n} e^{i\phi} \\ &= t_{i,R} \left(1 + \frac{t_{i,n}}{t_{i,R}} e^{i\phi} \right) \\ &= 1 + t_{i,n} e^{i\phi}, \end{aligned}$$

where we substitute $t_{i,R}$ to 1 without loss of generality. This leads the QRB-GS feedback $S_{i,n}(\phi)$:

$$\begin{aligned} S_{i,n}(\phi) &= |E_{i,n}^{\text{out}}(\phi)|^2 \times \Delta \sigma_i (\gamma_0 - \gamma_1) \\ &= [1 + t_{i,n}^2 + 2|t_{i,n}| \cos(\phi + \arg(t_{i,n}))] \\ &\quad \times \Delta \sigma_i (\gamma_0 - \gamma_1). \end{aligned}$$

By measuring the QRB-GS feedback with the four phase shifts $\phi = 0, \pi/2, \pi$, and $3\pi/2$, the phase of the matrix element is reconstructed by⁴⁰

$$\arg(t_{i,n}) = \arg \left[\frac{S_{i,n}(0) - S_{i,n}(\pi)}{4} + i \frac{S_{i,n}(3\pi/2) - S_{i,n}(\pi/2)}{4} \right].$$

S5. Phase Readout with Continuously-Driven ESR

We determine the phase of the transmission matrix element by sinusoidally modulating the optical excitation, as we sweep the phase of the incident basis modes relative to the reference mode. In the meantime, $\Delta \sigma$ with continuously-driven ESR depends on the optical excitation, since the steady-state solutions ρ and $E(\rho)$ of Eq. (S1) are a function of optical pumping³¹. This dependence produces non-linearity of the four-phase shift measurement with the QRB-GS feedback. In this section, we show the small variation of $\Delta \sigma$ does not affect on the phase readout in our measurement up to the first order.

For the holographic illumination $E_n^{\text{in}} = 1 + e^{i(\mathbf{k}_n \cdot \mathbf{r} + \phi)}$, the optical excitation $I_{i,n}(\phi)$ on the i th QRB is

$$I_{i,n}(\phi) = |E_{i,n}^{\text{out}}(\phi)|^2 = 1 + t_{i,n}^2 + 2t_{i,n} \cos(\phi + \theta_{i,n}),$$

where we substitute $\arg(t_{i,n})$ to $\theta_{i,n}$. We introduce the small variation of $\Delta \sigma$ up to the first order, while we modulate the phase ϕ of the holographic illumination:

$$\Delta \sigma_i(\phi) \simeq \Delta \sigma_i^{(0)} + \Delta \sigma_i^{(1)}(\phi)$$

where

$$\begin{aligned} \Delta \sigma_i^{(0)} &= \Delta \sigma_i \Big|_{I_{i,n}(0)} - I_{i,n}(0) \frac{d\Delta \sigma_i}{dI} \Big|_{I_{i,n}(0)} \\ \Delta \sigma_i^{(1)}(\phi) &= I_{i,n}(\phi) \frac{d\Delta \sigma_i}{dI} \Big|_{I_{i,n}(0)}. \end{aligned}$$

The corresponding QRB-GS feedback is

$$\begin{aligned} S_{i,n}(\phi) &= I_{i,n}(\phi) \Delta \sigma_i(\phi) (\gamma_0 - \gamma_1) \\ &= I_{i,n}(\phi) [\Delta \sigma_i^{(0)} + \Delta \sigma_i^{(1)}(\phi)] (\gamma_0 - \gamma_1) \\ &= S_{i,n}^{(0)}(\phi) + S_{i,n}^{(1)}(\phi), \end{aligned}$$

where

$$\begin{aligned} S_{i,n}^{(0)}(\phi) &= (\gamma_0 - \gamma_1) \Delta \sigma_i^{(0)} I_{i,n}(\phi) \\ &\doteq \alpha_{i,n}^{(0)} + \alpha_{i,n}^{(1)} \cos(\phi + \theta_{i,n}) \\ S_{i,n}^{(1)}(\phi) &= (\gamma_0 - \gamma_1) I_{i,n}(\phi)^2 \frac{d\Delta \sigma_i}{dI} \Big|_{I_{i,n}(0)} \\ &\doteq \beta_{i,n}^{(0)} + \beta_{i,n}^{(1)} \cos(\phi + \theta_{i,n}) + \beta_{i,n}^{(2)} \cos^2(\phi + \theta_{i,n}). \end{aligned}$$

Since $\cos^2(\theta_{i,n} + \pi) = \cos^2 \theta_{i,n}$ and $\cos^2(\theta_{i,n} + 3\pi/2) = \cos^2(\theta_{i,n} + \pi/2)$, the nonlinear dependence in the four phase measurement is cancelled out, resulting in

$$\begin{aligned} & \arg \left[\frac{S_{i,n}(0) - S_{i,n}(\pi)}{4} + i \frac{S_{i,n}(3\pi/2) - S_{i,n}(\pi/2)}{4} \right] \\ &= \arg \left[\frac{\alpha_{i,n}^{(1)} + \beta_{i,n}^{(1)}}{2} (\cos \theta_{i,n} + i \sin \theta_{i,n}) \right] \\ &= \arg(t_{i,n}). \end{aligned}$$

S6. Estimation of Spatial Resolution

Here, we describe how to estimate the spatial resolution of achieved subwavelength foci. Here, we assume the target QRB₁ and QRB₂ are point-like particles localized at \mathbf{x}_1 and \mathbf{x}_2 , respectively. In continuously-driven ESR spectroscopy, the spin density operators ρ_1 and ρ_2 are optically polarized into $|0\rangle\langle 0|$ when the microwave frequency ν_{off} is far off from their resonance frequencies, ν_1 and ν_2 . By contrast, when the microwave is on resonances with ν_1 and ν_2 , ρ_1 and ρ_2 become $(1 - \Delta\sigma)|0\rangle\langle 0| + \Delta\sigma|1\rangle\langle 1|$ with $\Delta\sigma = 1/2$, provided that the QRBs are not optically saturated³¹.

In this analysis, we denote $I_1^{(1)}$ and $I_2^{(1)}$ ($I_1^{(2)}$ and $I_2^{(2)}$) as the optical excitation at \mathbf{x}_1 and \mathbf{x}_2 when the wavefront W_{ν_1} (W_{ν_2}) is projected. $N^{(1)}(\nu)$ ($N^{(2)}(\nu)$) is the corresponding ODMR spectra with W_{ν_1} (W_{ν_2}) projection. To estimate the spatial resolution $\Delta r^{(1)}$ of the subwavelength focus at \mathbf{x}_1 with W_{ν_1} projection, we consider the relations,

$$N^{(1)}(\nu_{\text{off}}) = I_1^{(1)}\gamma_0 + I_2^{(1)}p\gamma_0 \quad (\text{S9})$$

$$\begin{aligned} N^{(1)}(\nu_1) &= I_1^{(1)}[\gamma_0(1 - \Delta\sigma) + \gamma_1\Delta\sigma] + I_2^{(1)}p\gamma_0 \\ &= I_1^{(1)}\left(\gamma_0 - \frac{\Delta\gamma}{2}\right) + I_2^{(1)}p\gamma_0 \end{aligned} \quad (\text{S10})$$

$$\begin{aligned} N^{(1)}(\nu_2) &= I_1^{(1)}\gamma_0 + I_2^{(1)}p[\gamma_0(1 - \Delta\sigma) + \gamma_1\Delta\sigma] \\ &= I_1^{(1)}\gamma_0 + I_2^{(1)}p\left(\gamma_0 - \frac{\Delta\gamma}{2}\right). \end{aligned} \quad (\text{S11})$$

Here, $\Delta\gamma = \gamma_0 - \gamma_1$, and the parameter p takes account of the NV density difference between the two QRBs.

p can be determined from ODMR $N^{(\text{cl})}(\nu)$ under the diffraction-limited excitation, in which the optical excitations at \mathbf{x}_1 and \mathbf{x}_2 are approximately equal:

$$p = \frac{N^{(\text{cl})}(\nu_{\text{off}}) - N^{(\text{cl})}(\nu_2)}{N^{(\text{cl})}(\nu_{\text{off}}) - N^{(\text{cl})}(\nu_1)}. \quad (\text{S12})$$

In our experiment, we determine p with W_{cl} projection.

From the ODMR spectra plotted in Fig. 4D, we obtain the ODMR at ν_{off} , ν_1 , and ν_2 by fitting to the Lorentzian lineshape function:

$$\begin{aligned} N^{(1)}(\nu_1)/N^{(1)}(\nu_{\text{off}}) &= 0.9902 \quad (0.9891, 0.9912) \\ N^{(1)}(\nu_2)/N^{(1)}(\nu_{\text{off}}) &= 0.9988 \quad (0.9976, 0.9999) \\ N^{(2)}(\nu_1)/N^{(2)}(\nu_{\text{off}}) &= 0.9994 \quad (0.9985, 1.0004) \\ N^{(2)}(\nu_2)/N^{(2)}(\nu_{\text{off}}) &= 0.9878 \quad (0.9870, 0.9885) \\ N^{(\text{cl})}(\nu_1)/N^{(\text{cl})}(\nu_{\text{off}}) &= 0.9954 \quad (0.9943, 0.9965) \\ N^{(\text{cl})}(\nu_2)/N^{(\text{cl})}(\nu_{\text{off}}) &= 0.9942 \quad (0.9932, 0.9952), \end{aligned}$$

where the values in the parenthesis represent 95% confidence bound of the fitting. By inserting the fit values to Eq. (S9-S12), we found $I_1^{(1)}/I_2^{(1)} \simeq 10.1$ and $p \simeq 1.261$. Similarly, $I_2^{(2)}/I_1^{(2)} \simeq 17.1$. Assuming subwavelength focus features a Gaussian intensity shape, its spatial resolution $\Delta r^{(1)}$ and $\Delta r^{(2)}$ are the FWHM of the intensity shapes:

$$\begin{aligned} \Delta r^{(1)} &= 2 \sqrt{\frac{\ln 2}{\ln(I_1^{(1)}/I_2^{(1)})}} \Delta x \simeq 204 \text{ nm} \\ \Delta r^{(2)} &= 2 \sqrt{\frac{\ln 2}{\ln(I_2^{(2)}/I_1^{(2)})}} \Delta x \simeq 184 \text{ nm}, \end{aligned}$$

where $\Delta x = |\mathbf{x}_1 - \mathbf{x}_2| = 186 \text{ nm}$ (Fig. S3). We plot the uncertainties of the estimations in Fig. 4E.

-
- [1] Ivo M Vellekoop, Ad Lagendijk, and AP Mosk, ‘‘Exploiting disorder for perfect focusing,’’ *Nature photonics* **4**, 320–322 (2010).
 [2] EG Van Putten, D Akbulut, J Bertolotti, WL Vos, A Lagendijk, and AP Mosk, ‘‘Scattering lens resolves sub-100 nm structures with visible light,’’ *Physical review letters* **106**, 193905 (2011).
 [3] Jung-Hoon Park, Chunghyun Park, HyeonSeung Yu, Jimin Park, Seungyong Han, Jonghwa Shin, Seung Hwan Ko, Ki Tae Nam, Yong-Hoon Cho, and YongKeun Park, ‘‘Subwavelength light focusing using random nanoparticles,’’ *Nature photonics* **7**, 454–458 (2013).
 [4] S bastien Popoff, Geoffroy Lerosey, Mathias Fink, Albert Bocara, and Sylvain Gigan, ‘‘Image transmission through an opaque material,’’ *Nature Communications* **1**,

- 1–5 (2010).
 [5] Youngwoon Choi, Taeseok Daniel Yang, Christopher Fang-Yen, Pilsung Kang, Kyoung Jin Lee, Ramachandra R Dasari, Michael S Feld, and Wonshik Choi, ‘‘Overcoming the diffraction limit using multiple light scattering in a highly disordered medium,’’ *Physical review letters* **107**, 023902 (2011).
 [6] Chunghyun Park, Jung-Hoon Park, Christophe Rodriguez, HyeonSeung Yu, Minkwan Kim, Kyoungsuk Jin, Seungyong Han, Jonghwa Shin, Seung Hwan Ko, Ki Tae Nam, *et al.*, ‘‘Full-field subwavelength imaging using a scattering superlens,’’ *Physical review letters* **113**, 113901 (2014).
 [7] Roarke Horstmeyer, Haowen Ruan, and Changhuei Yang, ‘‘Guidestar-assisted wavefront-shaping methods for

- focusing light into biological tissue,” *Nature photonics* **9**, 563–571 (2015).
- [8] Ivo Micha Vellekoop, EG Van Putten, A Lagendijk, and AP Mosk, “Demixing light paths inside disordered metamaterials,” *Optics express* **16**, 67–80 (2008).
 - [9] Xiao Xu, Honglin Liu, and Lihong V Wang, “Time-reversed ultrasonically encoded optical focusing into scattering media,” *Nature photonics* **5**, 154–157 (2011).
 - [10] Ke Si, Reto Fiolka, and Meng Cui, “Fluorescence imaging beyond the ballistic regime by ultrasound-pulse-guided digital phase conjugation,” *Nature photonics* **6**, 657–661 (2012).
 - [11] Ying Min Wang, Benjamin Judkewitz, Charles A DiMarzio, and Changhui Yang, “Deep-tissue focal fluorescence imaging with digitally time-reversed ultrasound-encoded light,” *Nature communications* **3**, 928 (2012).
 - [12] Benjamin Judkewitz, Ying Min Wang, Roarke Horstmeyer, Alexandre Mathy, and Changhui Yang, “Speckle-scale focusing in the diffusive regime with time reversal of variance-encoded light (trove),” *Nature photonics* **7**, 300–305 (2013).
 - [13] Thomas Chaigne, Ori Katz, A Claude Boccara, Mathias Fink, Emmanuel Bossy, and Sylvain Gigan, “Controlling light in scattering media non-invasively using the photoacoustic transmission matrix,” *Nature Photonics* **8**, 58–64 (2014).
 - [14] Puxiang Lai, Lidai Wang, Jian Wei Tay, and Lihong V Wang, “Photoacoustically guided wavefront shaping for enhanced optical focusing in scattering media,” *Nature photonics* **9**, 126–132 (2015).
 - [15] Ori Katz, Eran Small, Yefeng Guan, and Yaron Silberberg, “Noninvasive nonlinear focusing and imaging through strongly scattering turbid layers,” *Optica* **1**, 170–174 (2014).
 - [16] Cheng Ma, Xiao Xu, Yan Liu, and Lihong V Wang, “Time-reversed adapted-perturbation (trap) optical focusing onto dynamic objects inside scattering media,” *Nature photonics* **8**, 931–936 (2014).
 - [17] Haowen Ruan, Mooseok Jang, and Changhui Yang, “Optical focusing inside scattering media with time-reversed ultrasound microbubble encoded light,” *Nature communications* **6** (2015).
 - [18] Gopalakrishnan Balasubramanian, IY Chan, Roman Kolesov, Mohannad Al-Hmoud, Julia Tisler, Chang Shin, Changdong Kim, Aleksander Wojcik, Philip R Hemmer, Anke Krueger, *et al.*, “Nanoscale imaging magnetometry with diamond spins under ambient conditions,” *Nature* **455**, 648 (2008).
 - [19] JR Maze, PL Stanwix, JS Hodges, S Hong, JM Taylor, P Cappellaro, L Jiang, MV Gurudev Dutt, E Togan, AS Zibrov, *et al.*, “Nanoscale magnetic sensing with an individual electronic spin in diamond,” *Nature* **455**, 644 (2008).
 - [20] Georg Kucsko, PC Maurer, Norman Ying Yao, MICHAEL Kubo, HJ Noh, PK Lo, Hongkun Park, and Mikhail D Lukin, “Nanometer scale thermometry in a living cell,” *Nature* **500**, 54 (2013).
 - [21] L Jiang, JS Hodges, JR Maze, P Maurer, JM Taylor, DG Cory, PR Hemmer, RL Walsworth, A Yacoby, AS Zibrov, *et al.*, “Repetitive readout of a single electronic spin via quantum logic with nuclear spin ancillae,” *Science* **326**, 267–272 (2009).
 - [22] Philipp Neumann, Johannes Beck, Matthias Steiner, Florian Rempp, Helmut Fedder, Philip R Hemmer, Jörg Wrachtrup, and Fedor Jelezko, “Single-shot readout of a single nuclear spin,” *Science* **329**, 542–544 (2010).
 - [23] Lucio Robledo, Lilian Childress, Hannes Bernien, Bas Hensen, Paul F. A. Alkemade, and Ronald Hanson, “High-fidelity projective read-out of a solid-state spin quantum register,” *Nature* **477**, 574–578 (2011).
 - [24] Hannes Bernien, Bas Hensen, Wolfgang Pfaff, Gerwin Koolstra, MS Blok, Lucio Robledo, TH Taminiau, Matthew Markham, DJ Twitchen, Lilian Childress, *et al.*, “Heralded entanglement between solid-state qubits separated by three metres,” *Nature* **497**, 86–90 (2013).
 - [25] Tim Hugo Taminiau, Julia Cramer, Toeno van der Sar, Viatcheslav V Dobrovitski, and Ronald Hanson, “Universal control and error correction in multi-qubit spin registers in diamond,” *Nature nanotechnology* **9**, 171–176 (2014).
 - [26] G Waldherr, Y Wang, S Zaiser, M Jamali, T Schulte-Herbrüggen, H Abe, T Ohshima, J Isoya, JF Du, P Neumann, *et al.*, “Quantum error correction in a solid-state hybrid spin register,” *Nature* **506**, 204–207 (2014).
 - [27] Norbert Kalb, Andreas A Reiserer, Peter C Humphreys, Jacob JW Bakermans, Sten J Kamerling, Naomi H Nickerson, Simon C Benjamin, Daniel J Twitchen, Matthew Markham, and Ronald Hanson, “Entanglement distillation between solid-state quantum network nodes,” *Science* **356**, 928–932 (2017).
 - [28] Florian Dolde, Ingmar Jakobi, Boris Naydenov, Nan Zhao, Sebastien Pezzagna, Christina Trautmann, Jan Meijer, Philipp Neumann, Fedor Jelezko, and Jörg Wrachtrup, “Room-temperature entanglement between single defect spins in diamond,” *Nature Physics* **9**, 139–143 (2013).
 - [29] Keigo Arai, Chinmay Belthangady, Huiliang Zhang, N Bar-Gill, SJ DeVience, Paola Cappellaro, Amir Yacoby, and Ronald Lee Walsworth, “Fourier magnetic imaging with nanoscale resolution and compressed sensing speed-up using electronic spins in diamond,” *Nature nanotechnology* **10**, 859–864 (2015).
 - [30] V Emiliani, F Intonti, M Cazayous, DS Wiersma, M Colocci, F Aliev, and A Lagendijk, “Near-field short range correlation in optical waves transmitted through random media,” *Physical review letters* **90**, 250801 (2003).
 - [31] A Dréau, M Lesik, L Rondin, P Spinicelli, O Arcizet, J-F Roch, and V Jacques, “Avoiding power broadening in optically detected magnetic resonance of single nv defects for enhanced dc magnetic field sensitivity,” *Physical Review B* **84**, 195204 (2011).
 - [32] Youngwoon Choi, Changhyeong Yoon, Moonseok Kim, Taeseok Daniel Yang, Christopher Fang-Yen, Ramachandra R Dasari, Kyoung Jin Lee, and Wonshik Choi, “Scanner-free and wide-field endoscopic imaging by using a single multimode optical fiber,” *Physical review letters* **109**, 203901 (2012).
 - [33] Eva Rittweger, Kyu Young Han, Scott E Irvine, Christian Eggeling, and Stefan W Hell, “Sted microscopy reveals crystal colour centres with nanometric resolution,” *Nature Photonics* **3**, 144–147 (2009).
 - [34] PC Maurer, JR Maze, PL Stanwix, Liang Jiang, Alexey Vyacheslavovich Gorshkov, Alexander A Zibrov, Benjamin Harke, JS Hodges, Alexander S Zibrov, Amir Yacoby, *et al.*, “Far-field optical imaging and manipulation of individual spins with nanoscale resolution,” *Nature Physics* **6**, 912–918 (2010).
 - [35] Vittorio Giovannetti, Seth Lloyd, and Lorenzo Maccone, “Advances in quantum metrology,” *Nature photonics* **5**, 222–229 (2011).
 - [36] Norman Y Yao, Liang Jiang, Alexey V Gorshkov, Peter C

- Maurer, Geza Giedke, J Ignacio Cirac, and Mikhail D Lukin, “Scalable architecture for a room temperature solid-state quantum information processor,” *Nature communications* **3**, 800 (2012).
- [37] Marcus W Doherty, Neil B Manson, Paul Delaney, Fedor Jelezko, Jörg Wrachtrup, and Lloyd CL Hollenberg, “The nitrogen-vacancy colour centre in diamond,” *Physics Reports* **528**, 1–45 (2013).
- [38] Ivo M Vellekoop and AP Mosk, “Focusing coherent light through opaque strongly scattering media,” *Optics letters* **32**, 2309–2311 (2007).
- [39] Joseph W Goodman, *Introduction to Fourier optics* (Roberts and Company Publishers, 2005).
- [40] SM Popoff, G Lerosey, R Carminati, M Fink, AC Boccara, and S Gigan, “Measuring the transmission matrix in optics: an approach to the study and control of light propagation in disordered media,” *Physical review letters* **104**, 100601 (2010).

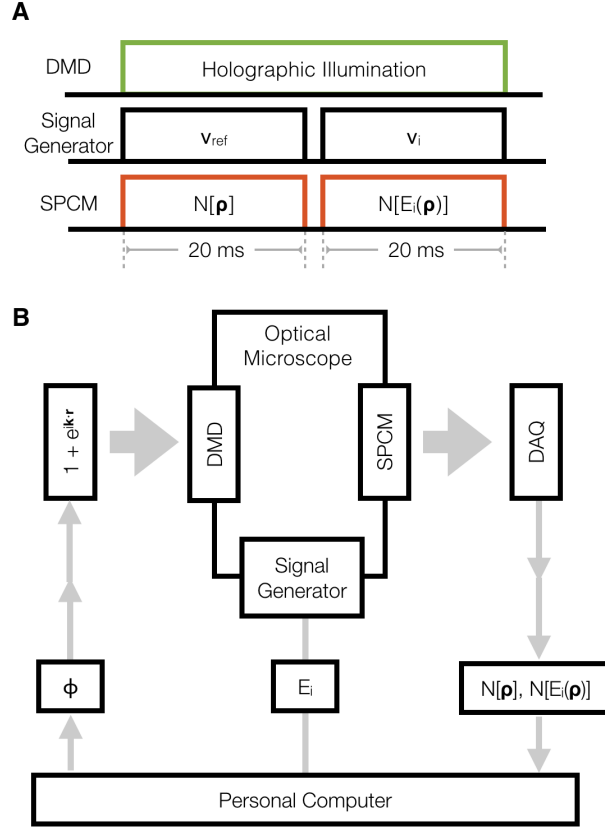


FIG. S1. **The QR-BGS feedback measurement sequences (A)** In our experiment, we modulate $\Delta\sigma_i$ of a target QRB with continuously-driven ESR. For a given holographic illumination, we continuously apply the microwave at the reference frequency of $\nu_{\text{ref}} = 2.5$ GHz, which is far off from $\nu_1 = 2.825$ GHz and $\nu_2 = 2.762$ GHz, for 20 ms, and at the target resonance frequency ν_1 or ν_2 for another 20 ms. During the microwave operations, we simultaneously collect the spin-dependent fluorescence photon $N[\rho]$ and $N[E(\rho)]$ with a single photon counting module. This unit sequence is repeated for 300 times per a holographic illumination. A digital clock pulse train from a DAQ synchronizes the microwave operations and the photon collections. **(B)** DMD in our optical microscope projects the holographic illumination $1 + e^{i\mathbf{k}\cdot\mathbf{r}}$ of the incident basis mode. Signal generator applies the quantum operator E to produce $\Delta\sigma_i$. SPCM counts the spin-dependent fluorescence photons, and DAQ returns the fluorescence measurement $N[\rho]$, $N[E(\rho)]$. From the measurements, personal computer determines the phase ϕ to be compensated on the incident basis mode. Updating the phase ϕ to DMD closes the iterative wavefront optimization cycle. DMD: digital micromirror device (D4100, Digital Innovations), SPCM: single photon counting module (SPCM-AQ4C, Excelitas), DAQ: Multi-functional data acquisition (NI-6343, National Instrument), Signal Generator (SME Rohde & Schwarz)

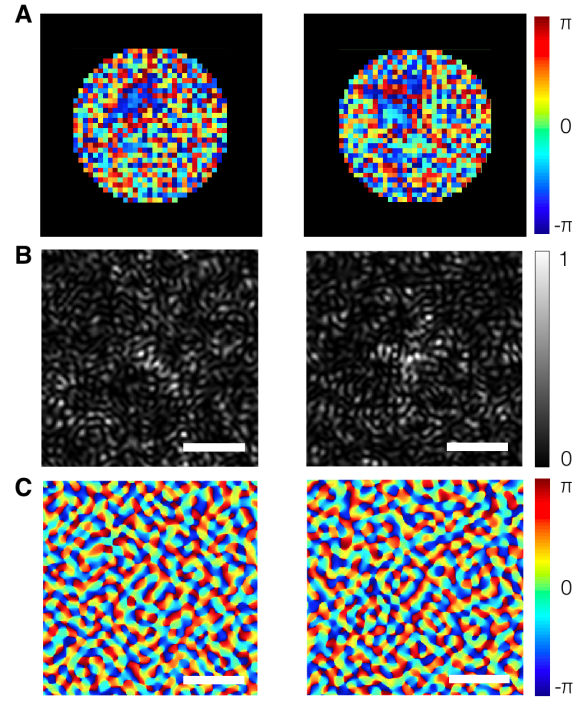


FIG. S2. **Incident wavefront shaping with the QRB-GS feedback** (Scale bars = 3 μm). **(A)** The phase maps of 793 incident basis modes, determined by the QRB-GS feedback. The DMD projects the phase maps into the back aperture of the excitation objective lens. Left (Right) plot is the result of the iterative optimization with the QRB-GS feedback at ν_1 (ν_2). **(B)** and **(C)**, The intensity and phase map of the incident wavefront on the complex medium, respectively. These maps are obtained by the Fourier transform of the phase maps plotted in **(A)**.

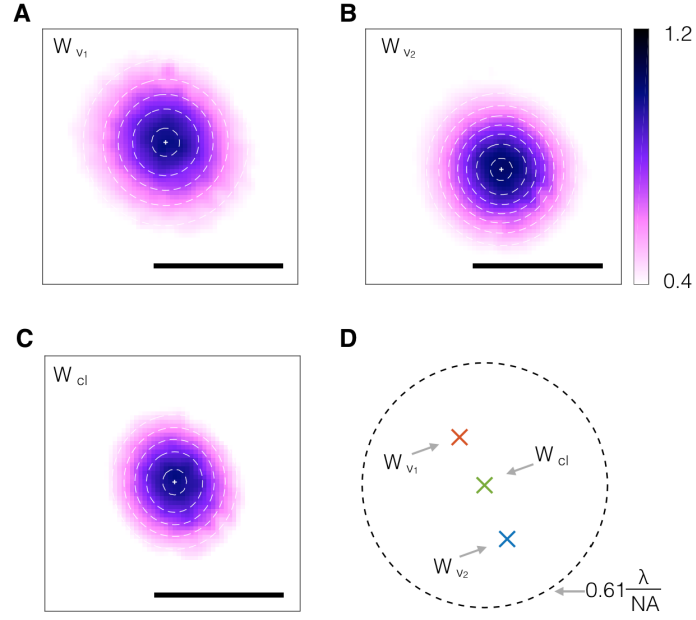


FIG. S3. **Sub-diffraction localization of target QRBs** (Scale bar = $1.22\lambda/NA \simeq 810$ nm). (A) and (B) We individually excite QRB_1 and QRB_2 with subwavelength optical focus through a scattering medium. The central position \mathbf{x}_1 and \mathbf{x}_2 of QRB_1 and QRB_2 are localized by fitting the recorded fluorescence images into two-dimensional Gaussian functions. (C) The central position with the W_{cl} projection for comparison. (D) Merged positions from (A), (B), and (C). The dashed circle guides the diffraction-limited resolution of the excitation microscope objective ($NA = 0.8$, $\lambda = 532$ nm).